This article has been accepted for publication in a future issue of this journal, but has not been fully edited. Content may change prior to final publication. Citation information: DOI 10.1109/TII.2018.2866804, IEEE Transactions on Industrial Informatics

Cell segmentation for quantitative analysis of anodized TiO2 foil

Hyun-Gyu Lee and Sang-Chul Lee, *Member, IEEE*

Abstract—We propose a quantitative analysis method using cell segmentation to evaluate the coating quality of anodic oxide. In order to identify each cell in a titania surface, a boundary region is adaptively detected according to the regional intensity distribution, and a boundary distance map is projected onto the scanning electron microscope (SEM) image of the titania surface. Each cell in the projected image is divided via clustering centered on the local maximum point. The uniformities of the cell distribution, size, and thickness are measured using the angle difference, size difference, and brightness difference between adjacent cells to comprehensively evaluate the quantitative alignment of the titania surface. The proposed method demonstrates the best performance in both cell detection and cell segmentation for SEM images of the titania surface compared with the state-of-the-art methods. The quantitative analysis of the anodic oxide film alignment was verified using color coding, histogram, and quantification of uniformity.

Index Terms—Cell segmentation, Quantitative analysis, TiO2 foil, Anodization, Ordering score.

1 Introduction

Anodization is a metal surface treatment technique that results in an artificial increase in the thickness of the oxide film on the metal surface to protect the metal or display various colors on the metal surface. The time, voltage, and temperature conditions of anodic oxidation are adjusted to obtain the required pore alignment, size, and shape, as shown in Fig. 1. Anodization may scatter and refract light, realize color, maximize the surface area, or waterproof the surface, depending on the alignment, size and shape of the pores in the nanotubes thus formed. Such nanostructures are used in various fields such as hydrogen production, solar cells, photocatalysts, anti-reflective coatings, lithium secondary batteries, and gas sensors [1]–[15].

Metals that produce protective coatings through anodic oxidation include aluminum, tantalum, magnesium, copper, and titanium [16]–[19]. Alumina, which is the most representative anodized metal, is widely used for decorative coatings of optical instruments, machine parts, household appliances, telecommunication equipment, etc. Anodized tantalum is an important acid-resistant material in the condenser and chemical industry, and it is used for nozzles for the production of fibers. Copper, which has good softness, has been used for decorative plating for a long time. Titanium, which forms a passive film in water or air near room temperature, and thus has high corrosion resistance similar to gold or platinum, is used in airplane parts. It is used for artificial joints, dental implants, ornaments, etc. due to biocompatible characteristics. In addition, anodized titania is used in dye-sensitized solar cells with a semiconductor electrode using nanotubes, and thus, it has a wide range of applications.

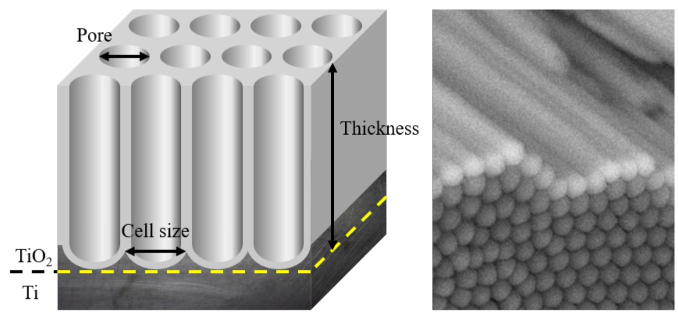

Fig. 1. Titania illustration and an SEM image of titania produced by anodization.

In recent years, new anodization techniques have been developed to produce various regular nanostructures on metal surfaces. The application range of anodization techniques has also extended to metals different from aluminum and titanium, which had been the focus of studies in the past. Anodic oxidation techniques have been thoroughly studied and defect detection techniques for a metal surface have been studied often [20]–[22], however, studies on methods for evaluating the degree of alignment of self-ordered oxides are relatively lacking.

Segmentation, quantification, and detection of nanomaterials such as nanofibrous and nanoparticles have attracted attention in industrial informatics [23], [24]. These techniques can be a foundation of for monitoring and automatic control systems, as well as predictive maintenance [25].

In general, an analytical method using a 2D Fourier transform of a scanning electron microscope (SEM) image is used to evaluate the alignment of a self-ordered porous material [26]–[28]. However, because the alignment evaluation method using the Fourier transform measures the approxi-

This work was supported by the National Research Foundation of Korea(NRF) grant funded by the Korea government(MSIT) (NRF-2018R1A2B6001643); This research was supported by Research Program To Solve Social Issues of the National Research Foundation of Korea(NRF) funded by the Ministry of Science and ICT. (No. NRF-2017M3C8A8091768)

Hyun-Gyu Lee is with Department of Computer Engineering, Inha University, 100 Inha-ro, Michuhol-gu, Incheon 22212, Korea (e-mail: ahye22@gmail.com).

Sang-Chul Lee is with Department of Computer Engineering, Inha University, 100 Inha-ro, Michuhol-gu, Incheon 22212, Korea (e-mail: sclee@inha.ac.kr).

This article has been accepted for publication in a future issue of this journal, but has not been fully edited. Content may change prior to final publication. Citation information: DOI 10.1109/TII.2018.2866804, IEEE Transactions on Industrial Informatics

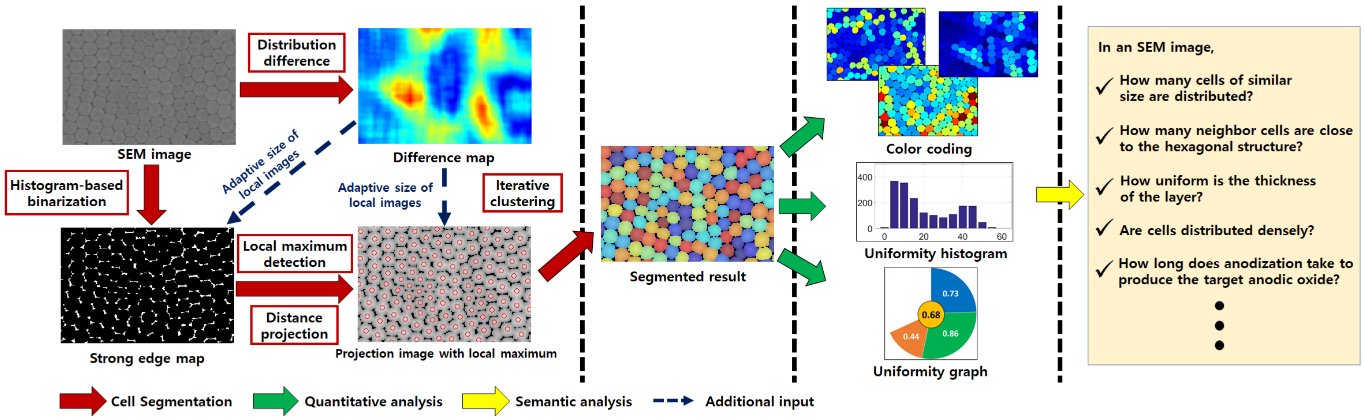

Fig. 2. Overview of cell segmentation-based proposed quantitative analysis.

mate characteristics of an entire image, it can not evaluate local characteristics, and its results can be unreliable in an environment where the imaging conditions are poor.

Threshold division, entropy-based fuzzy partitioning, and histogram-based adaptive partitioning have all been proposed in the last decade to quantitatively analyze images of porous structures [29]–[31]. Quantitative analysis using cell size, distance from the nearest cell, and an angle between nearest cells was also proposed; however, the only alumina with a defined cell and boundary was considered. Therefore, an expected result cannot be yielded from this method when analyzing an anodized titania thin film whose boundary is relatively ambiguous.

A cell estimation technique using 2D ray casting has been proposed for the cell division of microscopic images of such titania thin films [32], [33]. In a region where the boundary is ambiguous and difficult to estimate, cells can be found while repeatedly restoring the boundaries. However, the technique is limited in that a suitable cell must be estimated from within the candidate group owing to the method of finding the most suitable cell from among the estimated multiple cell candidates.

In this paper, we propose a quantitative method for analyzing the alignment of an anodized titania thin film using the cell segmentation of a distance map projected-image, as shown in Fig. 2. The proposed method adaptively detects a clear boundary in the nanotube according to the local distribution of pixel intensity, and it divides each cell by clustering the local maximum point in a projected image that combines the SEM image with the detected boundary and the boundary distance map. Finally, we evaluate the coating quality of titania by calculating the total uniformity, which measures the consistency of alignment through a combination of angle difference, size difference, and brightness difference between adjacent cells.

2 Related Works

A commonly used method for analyzing the porous structure of titania and alumina is the frequency domain-based method using Fourier transform [26]–[28]. A sharp peak in the 2D Fourier domain of the microscopic image indicates whether a long-range crystalline order property is present in the image, and the amplitude indicates the thickness of the layer. However, because the definition of a sharp peak is ambiguous, and it is not possible to quantitatively analyze the relationship between the long-range crystalline order and the position and amplitude in the 2D Fourier domain, our definition of the approximate characteristics of the entire image depends upon a human subjective judgment. Such a method, which shows the average characteristic of the alignment, is greatly influenced by the image noise of the SEM and the local ambiguity of the anodic oxide.

In order to overcome this problem, a method that recognizes each cell in an SEM image and analyzes it locally has been proposed [29]–[31]. Simple binarization-based cell identification by a threshold [29] enables the local analysis of the alumina in an SEM image, and it identifies the center point and contour of pores more precisely by applying an entropy-based automatic fuzzy binarization technique [30]. These methods cannot guarantee a meaningful performance for images where the contrast between the boundary and the pore is locally different. For the regional analysis of alumina images under the above-mentioned poor conditions, an adaptive binarization method using the brightness value of each pixel from a low-pass filtered image as a threshold value has been proposed [31]. However, this method is ideal for alumina images with sufficient distance between pores, and it is not suitable for titania images with relatively small pore distances.

In general, the active contour model (ACM) method [32]–[35] is used for object contour recognition. However, in order to apply the ACM technique to cell segmentation of the titania image, the initial value of the region type is required for each cell, and this technique requires time-consuming iterative calculations for each cell in SEM images containing a large number of cells [36].

Recently, existing morphological estimation-based segmentation techniques typically used with alumina images have been proposed for use with titania whose cell outlines are far more difficult to detect [36], [37]. These methods preferentially detect a clear boundary between adjacent cells and select the final cell among several candidate cells generated by two-dimensional ray casting. These methods use either a radial-based maximum roundness [36] selection method or a curvature-energy-based minimum roundness [37] selection method. To be successful, these two types

This article has been accepted for publication in a future issue of this journal, but has not been fully edited. Content may change prior to final publication. Citation information: DOI 10.1109/TII.2018.2866804, IEEE Transactions on Industrial Informatics

of roundness selection-based segmentation methods must produce adequate cells among the estimated cell candidates. It also cannot be guaranteed that the cell closest to the original shape in the candidate group is selected because the cell with the best roundness is not always the cell with the most optimal shape. Therefore, a new method of segmentation is needed to identify the shape of a cell more accurately whose boundaries are ambiguous in titania SEM images.

After each cell is divided, a quantitative analysis of self-ordered nanoarrays should be performed. In the alignment analysis of alumina images, the measurements of distance and angular deviation from surrounding cells are used as indices of the degree of alignment, while color coding and a histogram are used to visualize the alignment [29], [31]. However, unlike alumina images where pores of similar sizes should be detected, cell surfaces of various sizes are expected in the titania thin film. Therefore, additional analytical methods for angular deviation from surrounding cells and a comprehensive quantification technique are needed for titania images.

3 Cell segmentation for quantitative analysis

3.1 Boundary detection using local brightness distribution

Titania exhibits very dense cells throughout the SEM image, with very thin cell boundaries measuring about one to two pixels thick. Since classic edge detectors such as Sobel and Canny [38], [39] are sensitive to parameters and tend to generate double edges in the SEM image, an intensity-based edge detector with adaptive thresholding was proposed to avoid these issues [36], [37]. Although their edge detector cannot identify blurred or thin edges, it successfully minimizes the inaccurate detection of edge pixels in the grain region while maximizing the number of correctly detected strong pixels. The intensity-based edge detector $C(\cdot)$ is defined as follows [37]:

$$
\begin{aligned}
C(x,y) &= \begin{cases} 1, \text{if } \alpha(x,y) < I(x,y) \\ 0, \text{otherwise} \end{cases}, \\
\alpha(x,y) &= \underset{l\in[0,255]}{\arg\min} \left| \frac{1}{m^2} \left(\sum_{t=0}^{255} \sum_{u=-m/2}^{m/2} \sum_{v=-m/2}^{m/2} \Phi(x+u,y+v,t) \right) - \beta \right|, \\
\Phi(x+u,y+v,t) &= \begin{cases} 1, \text{if } I(x+u,y+v) = t \\ 0, \text{ otherwise} \end{cases},
\end{aligned}
\tag{1}
$$

where $C(x,y)$ is an indicator function that takes the value of one if the pixel at (x,y) represents the edge and zero otherwise by means of identifying edge pixels whose intensity is smaller than α. t is the pixel intensity related to a threshold, β is the rate of pixels that belong to edges in a $m \times m$ window, and $I(x+u,y+v)$ is the intensity of the pixel at $(x+u,y+v)$. The edge intensity is determined by α that indicates the threshold intensity (i.e., green bar) between the edge and the grain regions. $\Phi(x+u,y+v,t)$ indicates one when t is equal to the intensity of the pixel at $(x+u,y+v)$ and zero otherwise.

Although the previous edge detector [37] uses local images of the same size, the cell size and the thickness of the boundary vary according to anodization conditions, and thus, the ratio of the cell and the boundary may vary. Therefore, in this paper, we improved the method by adaptively changing the size of the local image according to the characteristics of the local brightness distribution. The difference $\Delta f(\cdot)$ between the brightness distribution of the whole image and the regional distribution determines the size of the local image, and it is defined as follows:

$$
\begin{aligned}
\Delta f(x,y) &= \sum_{i=1}^{n/2} (h_i(I) - h_i(I_{uv})) - \sum_{i=\frac{n}{2}+1}^{n} (h_i(I) - h_i(I_{uv})), \\
&\text{s.t. } x - \frac{b}{2} \le u \le x + \frac{b}{2},\ y - \frac{b}{2} \le v \le y + \frac{b}{2},
\end{aligned}
\tag{2}
$$

where $h_i(I)$ is the frequency of the i-th bin of the histogram for the entire image I, $h_i(I_{uv})$ is the i-th bin of the normalized histogram for the local image of the coordinates (u,v) corresponding to $\pm\frac{b}{2}$, and b is the fixed size of the local image. $h_i(I)$ and $h_i(I_{uv})$ are normalized histograms with a sum of one. The distribution difference $\Delta f(\cdot)$ contains negative values for which the lower bound is not determined. Therefore, $\Delta f(\cdot)$ is normalized for use as a weight, and the adaptive local size $w(\cdot)$ as follows:

$$
\begin{aligned}
w(x,y) &= \Delta f_{\text{norm}}(x,y)(b - b_{\text{low}}) + b_{\text{low}}, \\
\Delta f_{\text{norm}}(x,y) &= \begin{cases} 1, & \text{if } \Delta f_{\text{shift}}(x,y) > 1 \\ \Delta f_{\text{shift}}(x,y), & \text{otherwise} \end{cases}, \\
\Delta f_{\text{shift}}(x,y) &= \Delta f(x,y) - \min(\Delta f)
\end{aligned}
\tag{3}
$$

where the normalized distribution difference $\Delta f_{\text{norm}}(\cdot)$ is small in the region where the cell size is small or the area ratio of the cell and the boundary varies, and $\Delta f_{\text{norm}}(\cdot)$ is large in the region where the cell size is large and the boundary is clear, as shown in Fig. 3. b is the fixed size used in Eq. (2) and the upper-bound size of the local image, b_{low} is the lower-bound size of the local image, and $w(\cdot)$ is a parameter for adaptively adjusting the size of the local image. In order to find a clear boundary we define an improved pixel brightness-based edge detector $C^*(\cdot)$ using an adaptively-sized local image as follows:

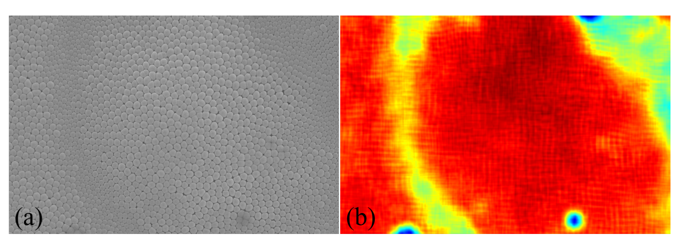

Fig. 3. (a) An SEM image and (b) brightness difference distribution Δf between the whole image and the local image. Warmer colors indicate a higher distribution difference.

This article has been accepted for publication in a future issue of this journal, but has not been fully edited. Content may change prior to final publication. Citation information: DOI 10.1109/TII.2018.2866804, IEEE Transactions on Industrial Informatics

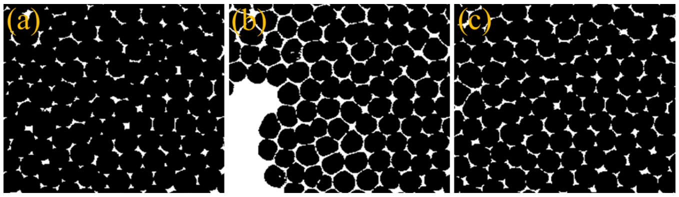

Fig. 4. Results produced by (a) [24], (b) Eq. (4), and (c) Eq. (5) using the same set of parameters.

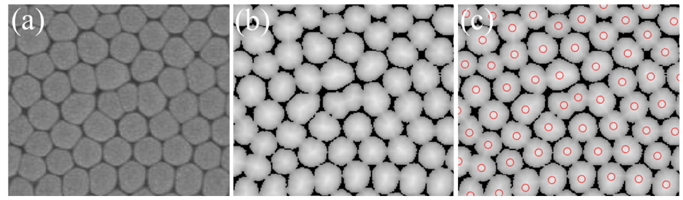

Fig. 5. (a) An SEM image, (b) distance projection image generated by (5), and (c) detected local maximum point (red circle).

$$
\begin{aligned}
C^*(x,y) &= \begin{cases} 1, \alpha(x,y) < I(x,y) \\ 0, \text{otherwise} \end{cases}, \\
\alpha(x,y) &= \underset{l\in[0,255]}{\arg\min} \Bigg| \frac{1}{w(x,y)^2} \\
&\left(\sum_{t=0}^{255} \sum_{u=-w(x,y)}^{w(x,y)} \sum_{v=-w(x,y)}^{w(x,y)} \Phi(x+u,y+v,t) \right) - \beta \Bigg|,
\end{aligned} \tag{4}
$$

where $\Phi(\cdot)$ is an indicator function equal to 1 if the pixel intensity is equal to l, and β is a parameter for adjusting the border ratio in a local image.

The improved intensity-based edge detector $C^*(\cdot)$ detects more adequate cell boundaries than the previous edge detector [37]. In combined with the $C^*(\cdot)$, we define the cumulative edge binarization $B(\cdot)$ to reduce the binarization noise, as follows:

$$
\begin{aligned}
B(x,y) &= \begin{cases} 1, \text{ if } B_{\text{norm}}(x,y) \geq \gamma \\ 0, \text{ otherwise} \end{cases}, \\
B_{\text{norm}}(x,y) &= \frac{B_{\text{acc}}(x,y)}{w(x,y)\max(B_{\text{acc}}/w)}, \\
B_{\text{acc}}(x,y) &= \sum_{u=-w(x,y)}^{w(x,y)} \sum_{v=-w(x,y)}^{w(x,y)} C^*(x+u,y+v),
\end{aligned} \tag{5}
$$

where $B(\cdot)$ is the binarized image for the boundary generated by the improved binarization technique, and γ is the threshold to produce the normalized cumulative binarized image $B_{\text{norm}}(\cdot)$.

As shown in Fig. 4, the proposed binarization according to Eq. (5) is less influenced by the anodization quality of the cell, cell size, and thickness of the boundary in comparison with the original binarization method, and is better able to extract a strong boundary line in the presence of noise in a better manner, compared with Eq. (4).

3.2 Cell segmentation of distance projected images

If the boundary region is removed from the image by the method proposed in Section 3.1, only the cell region remains in the image. In order to identify such a cell region as an individual cell, the cell is regarded as one cluster, and the number of cells is set to the number K of clusters in K-means clustering [40].

Our K-means clustering employs the features proposed in segmentation research on human U2OS cells [41], [42], defined in our case as the coordinates of each pixel in the cell region and the local maximum point coordinate. They consider each pixel in a region of interest (ROI) to be a feature of clustering. However, if only pixel coordinates are used, some pixels will be erroneously classified as those belonging to the other nuclei due to an elliptic shape of the nucleus. In [41], [42], this problem was solved by using the local maximum point coordinate of the original pixel estimated by the gradient ascent (GA) method. Starting from each position $\mathbf{x}$ in the ROI, GA ascends to a local maximum point following a path expressed by $\mathbf{x}^{k+1} = \mathbf{x}^k + \frac{r}{2}\nabla \mathrm{G}(\mathbf{x}^k)$, where $\nabla\mathrm{G}(\mathbf{x}^k)$ is the gradient at $\mathbf{x}^k$ in the Gaussian image G, k is the iteration number, and r is the step size. The GA method terminates when $\|\mathbf{x}^k - \mathbf{x}^{k+1}\|$ converges within a tolerance.

In order to increase the efficacy of the GA method, a projection image P that transforms the surface of the cell into a convex shape is generated through the combination of the original image and the distance map as follows:

$$
\begin{aligned}
P(\mathbf{x}) &= G(\mathbf{x}) + \frac{D(\mathbf{x})}{\max(D)}, \\
D(\mathbf{x}) &= \left\| \mathbf{x} - \underset{\mathbf{x}_{\mathrm{B}}}{\arg\min}(\mathbf{x} - \mathbf{x}_{\mathrm{B}}) \right\|, \ \mathbf{x}_{\mathrm{B}} \in \mathbf{B},
\end{aligned} \tag{6}
$$

where $G(\cdot)$ is the Gaussian blurred image, $\mathbf{x}$ is the (x,y) coordinates of the distance map $D(\cdot)$, and $\mathbf{B}$ is the set of coordinates $\mathbf{x_B}$ of the boundary detected by Eq. (5). The projection image P is defined as $\tilde{P}$ with the boundary region $B = 1$ set to 0, as shown in Fig. 5(b).

As shown in Fig. 5(b), the final projection image $\tilde{P}$ from which the boundary region is removed can detect a maximum point at a position near the center of the cell because the surface of the cell is convex. In the $\tilde{P}$, the local maximum point is used as the initial value of the cluster if the local maximum point is also the point of maximum brightness within the adaptive size range w, as follows:

$$
\begin{aligned}
\dot{\mathbf{x}} &= \{(x,y)|\tilde{P}(x,y) > \tilde{P}(u,v)\}, \\
\text{s.t. } u &\in [x - w(x,y),\ x + w(x,y)],\ u \neq x, \\
v &\in [y - w(x,y),\ y + w(x,y)],\ v \neq y
\end{aligned} \tag{7}
$$

As shown in Fig. 5(c), the center of most cells can be accurately detected by the variable local size. However, in a projection image, two or more center points may be extracted from some cells that are not transformed to the convex surface. In order to prevent such a problem, the upper bound b of Eq. (4), which determines the variable size $w(\cdot)$, is continuously reduced and clustered when a cell returns two or more center points in Algorithm 1. LMestimation in Algorithm 1 is a local maximum estimation

This article has been accepted for publication in a future issue of this journal, but has not been fully edited. Content may change prior to final publication. Citation information: DOI 10.1109/TII.2018.2866804, IEEE Transactions on Industrial Informatics

Algorithm 1. Iterative cell division

procedure ITERATIVE_DIVISION($\tilde{P}$, Δf_{norm}, b, b_{low})
Variable description and initialization:
  $\mathbf{X}$: coordinate set of cell region
  $\mathbf{X}_{\nabla}$: local maximum coordinate of $\mathbf{X}$
  $\dot{\mathbf{X}}$: cell seed to be used as initial cluster mean
  n: the number of local seeds
  c_i: i-th cluster consisted of coordinate elements
  $\mathbf{C}_{\dot{\mathbf{X}}}$: cluster set produced from $\dot{\mathbf{X}}$
Cell division:
  for $i \leftarrow b$, b_{low} **do**
    $\dot{\mathbf{X}}$ =LMestimation($\tilde{P}, \Delta f_{\text{norm},}, i$)
    $\mathbf{C}_{\dot{\mathbf{X}}}$ = kmeans($\mathbf{X}, \mathbf{X}_{\nabla}, \dot{\mathbf{X}}$), $c_i \in \mathbf{C}_{\dot{\mathbf{X}}}$
    for $\mathbf{j} \leftarrow \mathbf{1}$, $\mathbf{n}$ **do**
      if roundness$(c_i) > \delta$
        $\mathbf{C} \leftarrow c_i$
        remove elements of $\mathbf{X}$, $\mathbf{X}_{\nabla}$, and $\dot{\mathbf{X}}$, related to c_i
    end for
  end for
  return $\mathbf{C}$
end procedure

function that finds the position of initial point set $\dot{\mathbf{X}}$ of K-means clustering using Eq. (7). The number of initial points in $\dot{\mathbf{X}}$ is directly used as the number K of the cluster in K-means. The local maxima from the largest to the smallest scale are gradually used as the initial points of the K-means, and clusters having a shape satisfying the roundness of the cells are identified as cells. The identified local maximum points and the cells are excluded from the ROI when estimating the next scale. Eventually, we identify one cluster through K-means clustering as one cell.

The computational complexities of our boundary detection, image projection, and cell segmentation are $O(N_{\text{image}})$, $O(N_{\text{cell}}{N_{\text{area}}}^2+N_{\text{image}})$, and $O(N_{\text{image}}+N_{\text{cell}}N_{\text{area}})$, respectively, where N_{image} is an image size, N_{cell} is the number of cells in an image, and N_{area} is area of each cell. Therefore, the computational complexity of the whole cell segmentation algorithm is $O(N_{\text{image}} + N_{\text{cell}}N_{\text{area}} + N_{\text{cell}}{N_{\text{area}}}^2)$.

4 Quantitative analysis for uniformity

Various features have been suggested to define the image or object characteristics for decades, and the features are selected and modified to better explain training model in supervised learning [43], [44]. In feature selection such as PCA, l_2-norm is the most common least square loss function and is easily implemented. Compared with l_2-norm based loss function that is sensitive to outliers, $l_{2,1}$-norm based loss function showed good performance in dealing with noisy data. The loss functions are used in dimension reduction and unsupervised feature selection to decrease the computational cost for high dimensional data and to improve accuracy in processing noisy data. However, these are not suitable to assess uniformity or ordering scores of the titania thin films, because our study is to quantify uniformity and directly visualize it. In titania thin films, the surface of the thin film consists of cells that are distinct from alumina pores. Therefore, in order to analyze the surface, we propose metrics for cell size and thickness uniformity, as well as a quantitative analysis [29], [31] using the standard deviation of the angles between adjacent cells.

The brightness of a surface in an SEM image is related to several conditions, including the luminance and direction of the light source, the distance between the lens and the thin film, and the normal vector of the thin film surface. All surfaces are the same metal and therefore, they have the same properties. Thus, eliminating conditions related to the properties of the metal, the brightness of each pixel is described by the formula $L = L_{\text{amb}} + \frac{1}{(a_c+a_l d+a_q d^2)}(L_{\text{diff}} + L_{\text{spec}})$ for light attenuation along the distance d [45], where $L_{\text{amb}}, L_{\text{diff}}$, and L_{spec} are the ambient light, diffuse reflections and specular reflection, respectively, and a_c, a_l, and a_q are the light source attenuation factors depending on the distance.

It is assumed that each cell is influenced by the same light source in view of the characteristic of reflected light appearing on the whole cell surface in the image. Our uniformity analysis of the cell thickness considers the relative distance rather than the absolute distance between the lens and the thin film during imaging; therefore, the attenuation factor can be ignored in our method. Thus, L for distance and brightness can be approximated in a linear form. We propose an evaluation metric for uniformities of layer thickness, cell distribution, and size by measuring the depth difference Δd between neighboring cells using a linear approximation of L, the standard deviation σ for the angle between adjacent cells, and the size difference $\Delta\sigma$ between neighboring cells.

$$\begin{aligned}
\Delta d_i &= \sqrt{\sum_{j=1}^{N}(d_i - d_{i,j})^2}, \\
d &= \frac{\Omega}{\sum_s \sum_t (I(s,t) * K)}, \text{ s.t.} s,\ t \in \text{c}, \\
\sigma_i &= \sqrt{\frac{\sum_{i=1}^{N}(\theta_i - \bar{\theta})^2}{N-1}},\ \theta_i = \sin^{-1}\Big(\frac{v_i \cdot v_{i+1}}{\|v_i\|\|v_{i+1}\|}\Big), \\
\Delta\Omega_i &= \sqrt{\sum_{j=1}^{N}(\Omega_i - \Omega_{i,j})^2},
\end{aligned} \tag{8}$$

where N is the number of references of the nearest neighbor cells, v is a vector from the center of an target cell to the center of the adjacent cell, θ_i is the angle between the neighboring vector aligned clockwise or counterclockwise, $\bar{\theta}$ is the average of these inter-angles, (s,t) are coordinates belonging to the segmented cell c, $d_{i,j}$ is the inverse of the average brightness of the j-th cell among the neighbor cells of the i-th target cell, and Ω is the number of pixels in the cell. Based on the three proposed cell uniformity measurements, we define the distribution uniformity U_{angle}, size uniformity U_{size}, thickness uniformity $U_{\text{thickness}}$ and overall uniformity U_{total} of the whole SEM image as:

$$\begin{aligned}
U_{\text{total}} &= \frac{1}{3}(U_{\text{angle}} + U_{\text{size}} + U_{\text{thickness}}), \\
U_{\text{angle}} &= 1 - n^{-1}\sum_{i=1}^{n} w_\sigma \sigma_i, \\
U_{\text{size}} &= 1 - n^{-1}\sum_{i=1}^{n} w_\Omega \Delta\Omega_i, \\
U_{\text{thickness}} &= 1 - n^{-1}\sum_{i=1}^{n} w_d \Delta d_i,
\end{aligned} \tag{9}$$

This article has been accepted for publication in a future issue of this journal, but has not been fully edited. Content may change prior to final publication. Citation information: DOI 10.1109/TII.2018.2866804, IEEE Transactions on Industrial Informatics

where n is the number of divided cells, and w_σ, w_Ω, and w_d are weight parameters that normalize the range of each uniformity.

The computational complexity of each uniformity evaluation is $O(N_{\text{cell}} N_{\text{area}})$.

5 Experimental Results

5.1 Experimental setup and tested algorithms

Ten 1280×860-pixel SEM images of titania thin films were prepared using different anodization times, as shown in Fig. 6. The ground truth, in which the cell and boundary regions of the titania image were discriminated by domain experts, was constructed to measure the cell detection and segmentation accuracy of the proposed method. Further, we compared the cell detection and segmentation accuracy of the proposed method with model-based cell segmentation methods [36], [37] which were developed for application to the titania images. All parameters in both methods were set to those proposed by their authors. To compare with segmentation methods used in cell segmentation, we tested two methods: graph-based modular interactive nuclear segmentation (MINS) [46] and interactive learning (ilastik) [47]. MINS produces promising segmentation results through parameters tuning, and ilastik yields adequate results through feature extraction and learning. In the comparison experiment, parameters in MINS were empirically set, and the intensity, edge, and texture were used as features in ilastik. All experiments were performed on a PC with an Intel i7 CPU running at 2.3 GHz and with 8 GB of memory.

5.2 Performance evaluation for cell detection

The parameters b, b_{low}, and the binarization threshold γ represent the local image size in Eqs (2), (4), and (5), respectively, used to find clear boundaries. These parameters were set to 50, 8, and 0.06, respectively, just as with the previous boundary detection method [36]. The parameters b, b_{low}, and δ of Algorithm 1 were set to 12, 5, and 0.8, respectively.

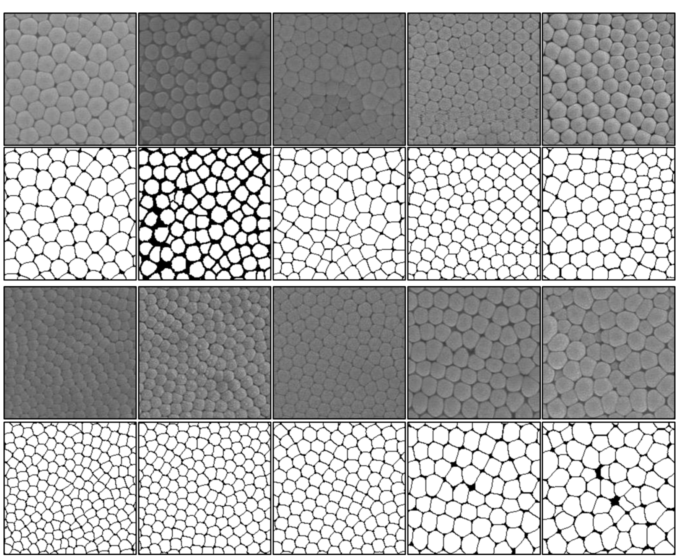

Fig. 6. Examples of ten SEM images and their ground truth used in the experiments.

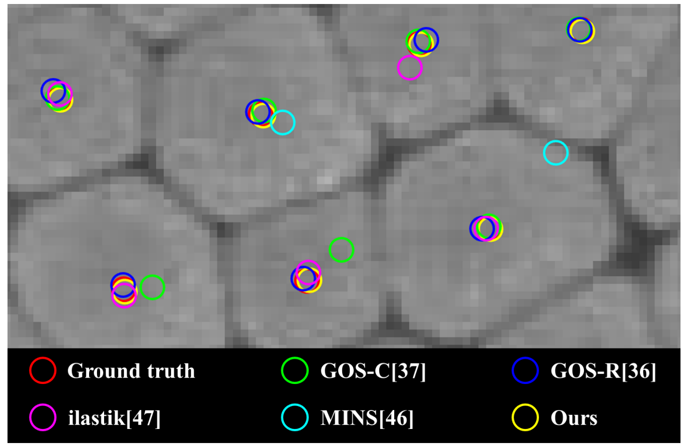

Fig. 7. Cell centers detected by the proposed method and other cell detection methods.

As shown in Fig. 7, the center coordinates of the cell detected by the proposed method were consistently nearest to the ground truth coordinates when compared with the other methods. To quantitatively evaluate the result of cell detection, the segmented cells with the cell centers located within 8 pixels from the cell center coordinate of the ground truth were defined as true positive (tp), and otherwise defined as false positive (fp). The segmented cells without a cell center located within 8 pixels from the cell center of the ground truth were defined as false negative (fn). The proposed method detected the center position of the cell more accurately than the state-of-the-art cell detection methods, achieved higher precision and recall, and demonstrated the best performance in terms of cell counting, as summarized in Table 1. However, the general cell segmentation methods [46], [47] failed to yield reliable results to be used in quantitative analysis.

5.3 Performance evaluation for cell segmentation

In terms of cell segmentation accuracy, the result of the proposed method was the most similar to the ground truth. Morphological estimation methods using ray casting [36], [37] did not detect some cells and generated smooth contours that merged other cells together as shown in Fig. 8. The following three similarity measures were used for the quantitative analysis of cell segmentation accuracy.

TABLE 1
Performance evaluation for cell detection: MEAN and STD are the average distance and standard deviation between the center coordinates of the ground truth and the segmented cells belonging to tp, respectively; PRE and REC are the precision and recall, respectively. Bold text indicates the highest performance for each evaluation method.

	MEAN	STD	PRE	REC
MINS [46]	4.100	1.880	0.816	0.214
ilastik [47]	1.311	1.459	0.809	0.678
GOS-C [37]	2.358	1.901	0.887	0.769
GOS-R [36]	1.187	1.228	0.955	0.907
Ours	**0.824**	**0.575**	**0.997**	**0.989**

This article has been accepted for publication in a future issue of this journal, but has not been fully edited. Content may change prior to final publication. Citation information: DOI 10.1109/TII.2018.2866804, IEEE Transactions on Industrial Informatics

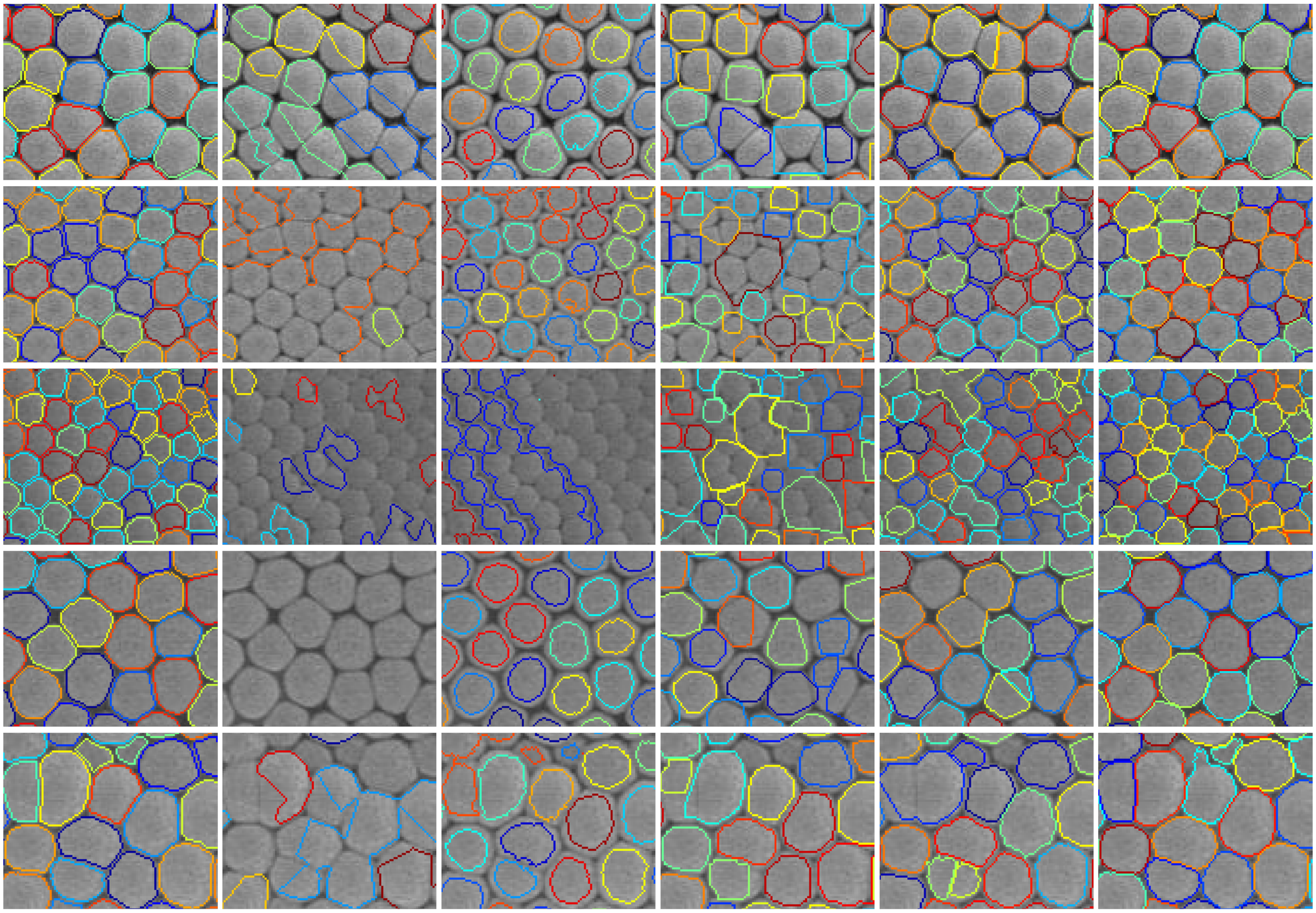

Fig. 8. Cell segmentation results produced by the proposed method and other methods.

$$\begin{aligned} Sensitivity(SEN) &= \frac{|R \cap S|}{|R|}, \\ Jaccard\,index(JAC) &= \frac{|R \cap S|}{|R \cup S|}, \\ Dicesimilarity\,coefficient(DSC) &= \frac{2|R \cap S|}{|R| + |S|}, \end{aligned} \tag{10}$$

where S and R are the segmented cells belonging to tp and the ground truth, respectively.

As listed in Table 2, the proposed method achieves high sensitivity; this implies that it detects the cell area very accurately. The Jaccard index and the dice similarity coefficient were also the highest for the proposed method, implying that it returns the most accurate detection of the cell area while maintaining a low false detection rate in the borderline area. Although the proposed method was slowest among the comparison methods, it is suitable for the segmentation for quantitative analysis because accurate segmentation is required to locally analyze the SEM image.

TABLE 2
Performance evaluation for cell segmentation. Comp.Time(s) is the average computation time of each method for an image.

	SEN	JAC	DSC	Comp.Time(s)
MINS [46]	0.723	0.594	0.741	26.4
ilastik [47]	0.686	0.652	0.786	**2.8**
GOS-C [37]	0.711	0.679	0.805	122.7
GOS-R [36]	0.886	0.844	0.915	210.1
Ours	**0.980**	**0.890**	**0.941**	599.2

5.4 Quantitative analysis of the titania alignment

In order to evaluate the degree of alignment of the titania thin film, the number N of the nearest neighbor cells was set to 6 as in the quantitative analysis study of alumina [29], [31]. The weights w_σ, w_Ω, and w_d of the three uniformities of the anodic oxide proposed in Eq. (9) were set to $\frac{1}{80}$, $\frac{1}{1200}$, and 20, respectively. The average computation time of alignment analysis was 91.48 sec for each image.

Fig. 9 shows the distribution, size, and thickness uniformity of cells using color coding, histogram, and uniformity graphs resulting from the proposed quantitative analysis method for the anodic oxide alignment. In the color-coded images, the cold colors represent a relatively low uniformity value, and the warm colors represent a relatively high uniformity value. In this way, it is possible to intuitively

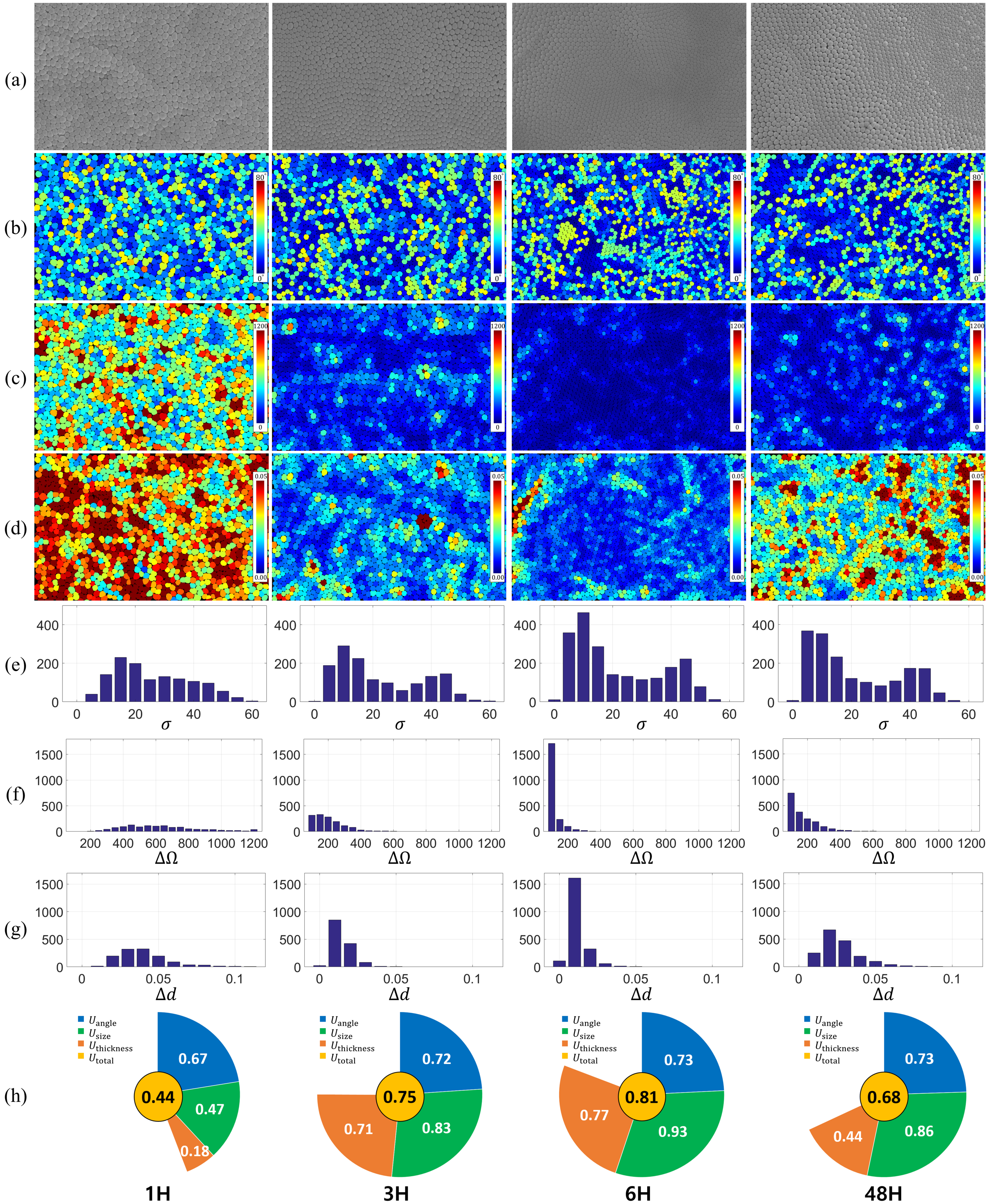

Fig. 9. The results of analysis of oxide alignment by uniformity analysis of segmented cells. Each column shows the image of a titania thin film anodized for 1 hour, 3 hours, 6 hours, or 48 hours, respectively, and its quantitative analysis. (a) SEM images of titania, color-coded images for uniformities of (b) cell distribution, (c) cell size, and (d) cell thickness; uniformity histograms of (e) distribution, (f) size, and (g) thickness; and (h) quantification of the uniformity of anodic oxide in the whole image.

This article has been accepted for publication in a future issue of this journal, but has not been fully edited. Content may change prior to final publication. Citation information: DOI 10.1109/TII.2018.2866804, IEEE Transactions on Industrial Informatics

view the distribution, size and thickness uniformity of the cells of the oxide. Such characteristics are also expressed in the histogram. The image in the third column with the cold color regions with the largest area has the most even distribution of hexagonal structures as shown in the histogram. It is also possible to see that the cells of similar size are the most prevalent, their size is relatively small, and the thickness of the layer is flat. In terms of the anodic oxidation time, the degree of cell alignment increased with time up to 6 h, after which the alignment decreased again. The overall uniformity U_{total}, which comprehensively reflects the distribution, size, and thickness of the oxide, was the highest for the third-column image with the best alignment and was lowest for the image in the first column with the worst alignment.

6 Conclusion

In this paper, we proposed a quantitative analysis technique for the alignment of titania thin films through cell segmentation. Adaptive local binarization was used to detect the boundaries between the nanotubes, and each cell was recognized by clustering based on the local maximum point. The proposed method achieved higher accuracy than any existing titania cell detection and segmentation techniques. Following cell segmentation, the anodized titania surface was quantitatively analyzed using the proposed alignment and thickness uniformity evaluation method, the results of which were visualized for intuitive analysis. Through our quantitative analysis, we can extract semantic information such as ordering score, thickness uniformity, and required anodization time to make a target oxide, and so on.

The quantitative evaluation method of the surface quality of anodic oxides described in this study can be applied to other anodic oxides such as alumina, as well as titania. Our cell detection and segmentation method is highly accurate and can be easily combined with other kinds of quantitative evaluation methods. Since our method makes it possible to quantitatively evaluate the results of the anodic oxidation technique, which requires the formation of a self-aligned porous oxide structure close to the target shape and size, it can be used for the evaluation and automation in industrial applications such as hydrogen production and the fabrication of solar cells, photocatalysts, anti-reflective coatings, lithium secondary batteries, and gas sensors.

References

[1] P. Roy, S. Berger, and P. Schmuki, "Tio2 nanotubes: Synthesis and applications," *Angewandte Chemie International Edition*, vol. 50, no. 13, pp. 2904–2939, 2011.

[2] Z. Lockman, S. Ismail, S. Sreekantan, L. Schmidt-Mende, and J. L. MacManus-Driscoll, "The rapid growth of 3 m long titania nanotubes by anodization of titanium in a neutral electrochemical bath," *Nanotechnology*, vol. 21, no. 5, p. 055601, 2010.

[3] M. Paulose, G. K. Mor, O. K. Varghese, K. Shankar, and C. A. Grimes, "Visible light photoelectrochemical and waterphotoelectrolysis properties of titania nanotube arrays," *Journal of Photochemistry and Photobiology A: Chemistry*, vol. 178, no. 1, pp. 8–15, 2006.

[4] K. Raja, M. Misra, V. Mahajan, T. Gandhi, P. Pillai, and S. Mohapatra, "Photo-electrochemical hydrogen generation using bandgap modified nanotubular titanium oxide in solar light," *Journal of Power Sources*, vol. 161, no. 2, pp. 1450–1457, 2006.

[5] K. Raja, V. Mahajan, and M. Misra, "Determination of photo conversion efficiency of nanotubular titanium oxide photoelectrochemical cell for solar hydrogen generation," *Journal of Power Sources*, vol. 159, no. 2, pp. 1258 – 1265, 2006.

[6] Y.-g. Wang and Y.-y. Xia, "A new concept hybrid electrochemical surpercapacitor: Carbon/limn2o4 aqueous system," *Electrochemistry Communications*, vol. 7, no. 11, pp. 1138–1142, 2005.

[7] J. M. Perez-Blanco and G. D. Barber, "Ambient atmosphere bonding of titanium foil to a transparent conductive oxide and anodic growth of titanium dioxide nanotubes," *Solar Energy Materials and Solar Cells*, vol. 92, no. 9, pp. 997 – 1002, 2008.

[8] D.-J. Yang, H. Park, S.-J. Cho, H.-G. Kim, and W.-Y. Choi, "Tio2-nanotube-based dye-sensitized solar cells fabricated by an efficient anodic oxidation for high surface area," *Journal of Physics and Chemistry of Solids*, vol. 69, no. 5, pp. 1272 – 1275, 2008.

[9] M. Paulose, K. Shankar, O. K. Varghese, G. K. Mor, and C. A. Grimes, "Application of highly-ordered tio2 nanotube-arrays in heterojunction dye-sensitized solar cells," *Journal of Physics D: Applied Physics*, vol. 39, no. 12, pp. 2498–2503, 2006.

[10] K. G. Ong, O. K. Varghese, G. K. Mor, K. Shankar, and C. A. Grimes, "Application of finite-difference time domain to dye-sensitized solar cells: The effect of nanotube-array negative electrode dimensions on light absorption," *Solar Energy Materials and Solar Cells*, vol. 91, no. 4, pp. 250 – 257, 2007.

[11] P. Pillai, K. Raja, and M. Misra, "Electrochemical storage of hydrogen in nanotubular tio2 arrays," *Journal of Power Sources*, vol. 161, no. 1, pp. 524 – 530, 2006.

[12] M. Paulose, O. K. Varghese, G. K. Mor, C. A. Grimes, and K. G. Ong, "Unprecedented ultra-high hydrogen gas sensitivity in undoped titania nanotubes," *Nanotechnology*, vol. 17, no. 2, pp. 398–402, 2005.

[13] J. Macak, P. Barczuk, H. Tsuchiya, M. Nowakowska, A. Ghicov, M. Chojak, S. Bauer, S. Virtanen, P. Kulesza, and P. Schmuki, "Self-organized nanotubular tio2 matrix as support for dispersed pt/ru nanoparticles: Enhancement of the electrocatalytic oxidation of methanol," *Electrochemistry Communications*, vol. 7, no. 12, pp. 1417 – 1422, 2005.

[14] A. Motonari, M. Yusuke, H. Makoto, and Y. Susumu, "Formation of titania nanotubes with high photo-catalytic activity," *Chemistry Letters*, vol. 29, no. 8, pp. 942–943, 2000.

[15] S.-Z. Chu, S. Inoue, K. Wada, D. Li, H. Haneda, and S. Awatsu, "Highly porous (tio2sio2teo2)/al2o3/tio2 composite nanostructures on glass with enhanced photocatalysis fabricated by anodization and solgel process," *The Journal of Physical Chemistry B*, vol. 107, no. 27, pp. 6586–6589, 2003.

[16] S. Tajima, *Anodic Oxidation of Aluminum*. Boston, MA: Springer US, 1970, pp. 229–362.

[17] G. U., R. M., and D. H., "Tantalum as a material of construction for the chemical processing industry a critical survey," *Materials and Corrosion*, vol. 46, no. 12, pp. 689–700.

[18] L. Ang, T. Hor, G. Xu, C. Tung, S. Zhao, and J. Wang, "Decoration of activated carbon nanotubes with copper and nickel," *Carbon*, vol. 38, no. 3, pp. 363 – 372, 2000.

[19] X. Liu, S. Chen, J. K. Tsoi, and J. P. Matinlinna, "Binary titanium alloys as dental implant materialsa review," *Regenerative Biomaterials*, vol. 4, no. 5, pp. 315–323, 2017.

[20] D. Carrera, F. Manganini, G. Boracchi, and E. Lanzarone, "Defect detection in sem images of nanofibrous materials," *IEEE Transactions on Industrial Informatics*, vol. 13, no. 2, pp. 551–561, 2017.

[21] M. Win, A. R. Bushroa, M. A. Hassan, N. M. Hilman, and A. Ide-Ektessabi, "A contrast adjustment thresholding method for surface defect detection based on mesoscopy," *IEEE Transactions on Industrial Informatics*, vol. 11, no. 3, pp. 642–649, 2015.

[22] B. Gao, W. L. Woo, G. Y. Tian, and H. Zhang, "Unsupervised diagnostic and monitoring of defects using waveguide imaging with adaptive sparse representation," *IEEE Transactions on Industrial Informatics*, vol. 12, no. 1, pp. 405–416, 2016.

[23] Z. Wang, "A new approach for segmentation and quantification of cells or nanoparticles," *IEEE Transactions on Industrial Informatics*, vol. 12, no. 3, pp. 962–971, June 2016.

[24] D. Carrera, F. Manganini, G. Boracchi, and E. Lanzarone, "Defect detection in sem images of nanofibrous materials," *IEEE Transactions on Industrial Informatics*, vol. 13, no. 2, pp. 551–561, April 2017.

[25] G. A. Susto, A. Schirru, S. Pampuri, S. McLoone, and A. Beghi, "Machine learning for predictive maintenance: A multiple classi-

fier approach," *IEEE Transactions on Industrial Informatics*, vol. 11, no. 3, pp. 812–820, June 2015.
[26] J. E. G. J. Wijnhoven and W. L. Vos, "Preparation of photonic crystals made of air spheres in titania," *Science*, vol. 281, no. 5378, pp. 802–804, 1998.
[27] C. Pacholski, M. Sartor, M. J. Sailor, F. Cunin, and G. M. Miskelly, "Biosensing using porous silicon double-layer interferometers: reflective interferometric fourier transform spectroscopy," *Journal of the American Chemical Society*, vol. 127, no. 33, pp. 11 636–11 645, 2005.
[28] W. J. Stpniowski, T. Durejko, M. Michalska-Domaska, M. aziska, and J. Aniszewska, "Characterization of nanoporous anodic aluminum oxide formed on laser pre-treated aluminum," *Materials Characterization*, vol. 122, no. Supplement C, pp. 130–136, 2016.
[29] R. Hillebrand, F. Mller, K. Schwirn, W. Lee, and M. Steinhart, "Quantitative analysis of the grain morphology in self-assembled hexagonal lattices," *ACS Nano*, vol. 2, no. 5, pp. 913–920, 2008.
[30] S. Mtfi-Tempfli, M. Mtfi-Tempfli, and L. Piraux, "Characterization of nanopores ordering in anodic alumina," *Thin Solid Films*, vol. 516, no. 12, pp. 3735 – 3740, 2008.
[31] M. J. Abdollahifard, K. Faez, M. Pourfard, and M. Abdollahi, "A histogram-based segmentation method for characterization of self-assembled hexagonal lattices," *Applied Surface Science*, vol. 257, no. 24, pp. 10 443–10 450, 2011.
[32] M. Shemesh and O. Ben-Shahar, *Free Boundary Conditions Active Contours with Applications for Vision*. Berlin, Heidelberg: Springer Berlin Heidelberg, 2011, pp. 180–191.
[33] C. Li, C. Xu, C. Gui, and M. D. Fox, "Distance regularized level set evolution and its application to image segmentation," *IEEE Transactions on Image Processing*, vol. 19, no. 12, pp. 3243–3254, Dec 2010.
[34] J. Mille, "Narrow band region-based active contours and surfaces for 2d and 3d segmentation," *Computer Vision and Image Understanding*, vol. 113, no. 9, pp. 946 – 965, 2009.
[35] O. Bernard, D. Friboulet, P. Thevenaz, and M. Unser, "Variational b-spline level-set: A linear filtering approach for fast deformable model evolution," *IEEE Transactions on Image Processing*, vol. 18, no. 6, pp. 1179–1191, June 2009.
[36] H. G. Lee, M. K. Choi, and S. C. Lee, "Grain-oriented segmentation of scanning electron microscope images," in *2013 IEEE International Conference on Image Processing*, Sept 2013, pp. 4029–4033.
[37] H.-G. LEE, M.-K. CHOI, and S.-C. LEE, "Grain-oriented segmentation of images of porous structures using ray casting and curvature energy minimization," *Journal of Microscopy*, vol. 257, no. 2, pp. 92–103, 2015.
[38] R. C. Gonzalez and R. E. Woods, *Digital Image Processing (3rd Edition)*. Upper Saddle River, NJ, USA: Prentice-Hall, Inc., 2006.
[39] J. Canny, "A computational approach to edge detection," *IEEE Trans. Pattern Anal. Mach. Intell.*, vol. 8, no. 6, pp. 679–698, Jun. 1986.
[40] J. A. Hartigan and M. A. Wong, "Algorithm as 136: A k-means clustering algorithm," *Journal of the Royal Statistical Society. Series C (Applied Statistics)*, vol. 28, no. 1, pp. 100–108, 1979.
[41] H. G. Lee and S. C. Lee, "Nucleus segmentation by merge and split of gaussian mixture based shape models," *IEEE Journal of Biomedical and Health Informatics*, vol. 22, no. 1, pp. 235–243, 2018.
[42] H. G. Lee, A. Orzikulova, B. G. Park, and S. C. Lee, "Modeling structural dissimilarity based on shape embodiment for cell segmentation," in *2017 IEEE International Conference on Image Processing*, Sept 2017, pp. 4029–4033.
[43] X. Chang, F. Nie, Y. Yang, C. Zhang, and H. Huang, "Convex sparse pca for unsupervised feature learning," *ACM Trans. Knowl. Discov. Data*, vol. 11, no. 1, pp. 3:1–3:16, 2016.
[44] F. Nie, H. Huang, X. Cai, and C. H. Ding, "Efficient and robust feature selection via joint $l_{2,1}$-norms minimization," in *Advances in Neural Information Processing Systems 23*, J. D. Lafferty, C. K. I. Williams, J. Shawe-Taylor, R. S. Zemel, and A. Culotta, Eds. Curran Associates, Inc., 2010, pp. 1813–1821.
[45] D. D. Hearn, M. P. Baker, and W. Carithers, *Computer Graphics with Open GL*, 4th ed. Upper Saddle River, NJ, USA: Prentice Hall Press, 2010.
[46] X. Lou, M. Kang, P. Xenopoulos, S. Munoz-Descalzo, and A.-K. Hadjantonakis, "A rapid and efficient 2d/3d nuclear segmentation method for analysis of early mouse embryo and stem cell image data," *Stem cell reports*, vol. 2, no. 3, pp. 382–397, 2014.
[47] C. Sommer, C. Straehle, U. Koethe, and F. A. Hamprecht, "ilastik: Interactive learning and segmentation toolkit," in *Biomedical Imaging: From Nano to Macro, 2011 IEEE International Symposium on*. IEEE, 2011, pp. 230–233.